

A comparison between anomalous 6-cm H₂CO absorption and CO(1-0) emission in the L1204/S140 region

Mónica Ivette Rodríguez^{1,2}

Tommy Wiklind^{1,3}

Ronald J. Allen¹

Vladimir Escalante²

Laurent Loinard²

¹*Space Telescope Science Institute, 3700 San Martin Drive, Baltimore, MD 21218, USA
monica, rjallen, wiklind@stsci.edu*

²*Centro de Radioastronomía y Astrofísica, Universidad Nacional Autónoma de México,
Apartado Postal 72 - 3, C.P. 58091, Morelia, Michoacán, México
m.rodriguez, l.loinard, v.escalante@astrosmo.unam.mx*

³*Affiliated with the Space Sciences Department of the European Space Agency*

ABSTRACT

We report observations of the dust cloud L1204 with the Onsala 25-m telescope in the 6 cm (1₁₁-1₁₀) transition of H₂CO. The observed region includes the S140 H α arc. This spectral line is seen here in absorption against the cosmic microwave background, indicating the presence of widespread warm molecular gas at intermediate densities. Overall, the distributions of H₂CO and CO (taken from the literature) are fairly similar, though significant differences exist at small scales. Most notably, while the CO peak is nearly coincident with the S140 H α arc, the maximum H₂CO absorption is clearly separated from it by a full 10' beam (~ 3 pc). We argue that these differences result from differing abundances and excitation requirements. The CO(1-0) line is more optically thick and more biased towards warm gas than the H₂CO 6 cm line. On the other hand, formaldehyde is more easily photodissociated and is, therefore, a poorer tracer of the molecular gas located immediately behind Photon Dominated Regions.

Subject headings: ISM: clouds — ISM: molecules – radio lines: ISM – stars: formation – galaxies: ISM

1. Introduction

Since H_2 –the most abundant molecule in space– lacks a permanent dipole moment, its rotational transitions are prohibited. Although the quadrupolar transitions exist, they are of little use for the study of the bulk of molecular gas in the ISM because they require high temperature to be excited. Instead, the structure and properties of cold molecular clouds in the interstellar medium are usually studied using low-energy rotational transitions of simple non-symmetric polar molecules. For practical reasons, the first rotational transition ($J = 1 \rightarrow 0$) of carbon monoxide (CO), at 115.27 GHz has been the most popular choice. This transition, however, has long been known to be nearly always optically thick, so – for a given filling factor– its intensity is expected to increase monotonically with the kinetic temperature of the emitting gas. Clearly, this could have adverse effects on efforts to establish the distribution of molecular gas in the ISM from CO observations alone, because very low temperature gas might go unnoticed in sensitivity-limited CO observations while warm regions ($\gtrsim 20$ K) will stand out even if they are not those with the highest molecular content. The sources where these effects might be most noticeable are those with large temperature gradients; for instance in molecular clouds located in the immediate vicinity of hot stars.

While all molecular emission tracers share this temperature dependence to some degree, *absorption* lines can be detected even in very cold gas, provided sufficiently bright background continuum sources are available. The scarcity of such sources at the wavelength of the common molecular tracers, however, has limited the usefulness of absorption measurements in the study of specific Galactic molecular clouds (e.g Evans et al. 1980). The 6-cm (1_{10} - 1_{11}) transition of ortho formaldehyde (H_2CO) offers an interesting alternative. Owing to collisions with neutral particles that selectively overpopulate the lower energy level, the excitation temperature of the $1_{10} \rightarrow 1_{11}$ transition lies below 2.7 K (Townes & Cheung 1969). This allows the transition to be observed in absorption against the cosmic microwave background (CMB) (Snyder et al. 1969), and makes it a potentially powerful tracer of molecular gas in any direction of the sky. The excitation requirements are such the the 6 cm H_2CO line is a good indicator of the presence of cool to warm molecular gas ($T \gtrsim 10$ K) at intermediate densities ($10^3 \text{ cm}^{-3} \leq n \leq 10^5 \text{ cm}^{-3}$). Unfortunately, the absorption line is weak, so very large amounts of telescope time are required to map large areas of the sky.

Recently, Rodríguez et al. (2006) conducted a blind search for H_2CO absorption and compared CO emission and H_2CO absorption profiles towards the Galactic anticenter. They found a rough, large-scale correlation between these two tracers, and concluded that both lines preferentially trace warm and dense molecular gas. Here, we will examine this relation between CO and H_2CO at a somewhat smaller scale using observations of the well-known, nearby star-forming region Sharpless 140 (S140 –Sharpless 1959) associated with the dark

dust cloud Lynds 1204 (L1204 –Lynds 1962). L1204 is centered at $l = 107^{\circ}47$, $b = +4^{\circ}82$ and covers an area of 2.5 square degrees (Lynds 1962). At its southwest edge lies S140, a prominent compact arc-shaped H II region with an angular size of $\sim 2' \times 6'$. The ionization of S140 is maintained by the nearby B0V star HD211880 (Blair et al. 1978). The distance of S140/L1204 deduced from the brightness of the exciting star is 910 pc (Crampton & Fisher 1974). S140 has been the subject of many observational studies, that have usually focused on the Photon Dominated Region (PDR) on the edge of L1204, and on the embedded infrared sources located right behind it (e.g., Preibisch et al. 2001; Hayashi & Murata 1992; Preibisch & Smith 2002; Bally et al. 2002). Remarkably, while the dust cloud is seen as an extended dark feature covering more than two square degrees, the CO emission peaks immediately behind the H α arc (Heyer et al. 1996; Evans et al. 1987; Blair et al. 1978), while only relatively faint emission extends deep within the dust cloud (Helfer & Blitz 1997). The 6-cm line of H₂CO was detected in absorption against the CMB in L1204 near S140 by Blair et al. (1978) with the NRAO 43 m telescope, and unexpectedly by Evans et al. (1987) during VLA observations of the bright condensation just northwest of S140. However neither of those studies provided a extensive mapping of the H₂CO CMB absorption in L1204, and the exact extension of the gas traced by H₂CO remains unclear. In this article, we will present such a extensive mapping of the 6 cm CMB absorption of H₂CO over most of the large dust complex L1204, and compare our results with existing CO observations taken from the literature.

2. Data

The H₂CO observations were obtained during two sessions (January and September-October 2004, respectively) with the 25.6-m telescope of the *Onsala Space Observatory* (OSO) in Sweden. At 6 cm, the angular resolution is 10', and our pointing precision was always better than 20". Frequency-switching, with a frequency throw of 0.4 MHz was used, and both polarizations of the incoming signal were recorded simultaneously in two independent units of the autocorrelation spectrometer. Each of these units provided 800 2 kHz-wide channels. At the observed frequency of 4829.660 MHz, this setup provided a total bandwidth of 99 km s⁻¹ and a (Hanning-smoothed) velocity resolution of 8 kHz \equiv 0.49 km s⁻¹. The spectrometer was centered at the systemic velocity of S140, $V_{LSR} = -8.0$ km s⁻¹. Daily observations of the supernova remnant Cas A were used to check the overall performance of the system. The system temperature during our observations varied from 33 to 36 K.

In order to map the entire region behind S140, we observed 72 positions on a regular square grid with a 10' spacing, centered at $l = 107^{\circ}0$, $b = +5^{\circ}3$; the resulting map uniformly covers a $1^{\circ}0 \times 1^{\circ}8$ rectangular region (Fig. 1) . The off-line data reduction was done

with the CLASS program of the GILDAS software package (Guilloteau & Forveille 1989), and involved only the subtraction of (flat) baselines from individual integrations and the averaging of all spectra taken at the same pointing position. The total integration time for each of these positions was about 10 hours, yielding a typical final noise level of 3 mK (T_A^*).

The distribution of radio continuum sources in the region of L1204 has been studied in detail by Allen Machalek & Jia (in preparation), using data from the Canadian Galactic Plane Survey. Fairly bright continuum emission is associated with the $H\alpha$ arc and the embedded massive protostars located behind it –but, as we will see momentarily no formaldehyde was detected from either of these regions. In addition, a number of extragalactic background sources as well as diffuse emission associated with the dust cloud L1204 itself contribute to the overall radio continuum. The typical brightness temperature average over the Onsala beam at 6 cm, however, is only about 0.2 K, except towards the $H\alpha$ arc and the embedded massive protostars (where again, no absorption was detected). Since the brightness temperature is so small, any H_2CO absorption profiles features detected must be absorption of the cosmic microwave background radiation at 2.7 K.

In the analysis of our new observations, we will also make use of $^{12}CO(1-0)$ observations of L1204/S140 kindly provided by Dr. Tamara Helfer, and published in Heyer et al. (1996), and Helfer & Blitz (1997). These data were obtained with the 14-m telescope of the *Five College Radio Astronomy Observatory* (FCRAO) in Amherst (MA), and have an intrinsic angular resolution of $45''$. For comparison with our formaldehyde data, we have smoothed the $CO(1-0)$ observations to $10'$, and resampled them on our observing grid.

3. Results

Formaldehyde absorption was detected in at least 16 of our 72 observed positions (see Fig. 2). The maximum absorption is located $10'$ arcmin behind the S140 HII region at a LSR velocity of -8.0 km s^{-1} , similar to that of the CO emission detected in that area.

Table 1. Source positions.

Source	Position (l, b)	Size ($\Delta\alpha, \Delta\delta$)	$\alpha(J2000.0), \delta(J2000.0)$	Reference
L1204	$107^\circ 37', +4^\circ 87'$	$1^\circ 0' \times 2^\circ 5'$	$22^h 26^m 41^s + 63^\circ 15' 36''$	Lynds (1962)
S140(H_α)	$106^\circ 8', +5^\circ 3'$	$2' \times 6'$	$22^h 19^m 23^s + 63^\circ 18' 16''$	Sharpless (1959)
Our survey	$107^\circ 0', +5^\circ 3'$	$1^\circ 0' \times 1^\circ 8'$	$22^h 20^m 52^s + 63^\circ 24' 49''$	This paper

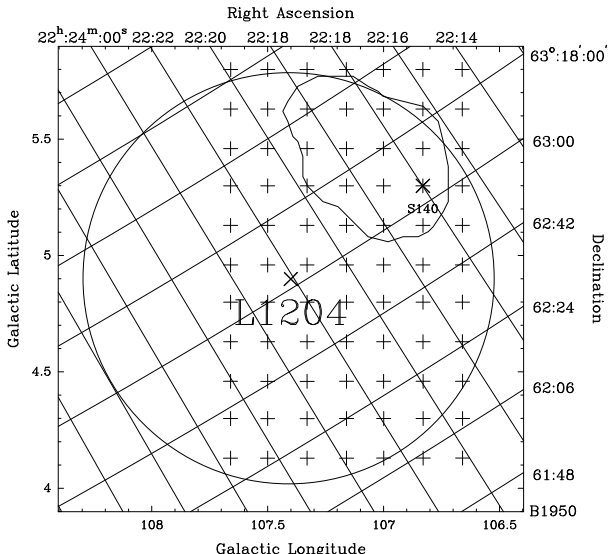


Fig. 1.— This figure shows a sketch of the L1204/S140 region, with our observed positions shown as “+” symbols. The correspondence between Galactic coordinates (used throughout the paper) and equatorial coordinates (that have usually been preferred for observations of S140) is indicated. The circle represents the $2^{\circ}5'$ size of the dust cloud L1204 as reported by Lynds (1962). The central positions of L1204 and S140 are shown as “+” symbols. The contour represents the lowest value of the H_2CO absorption.

A second spatio-kinematical structure is detected towards the north-east (here, and in the rest of the paper, north and all other directions refer to Galactic coordinates), at $V_{LSR} \sim -11 \text{ km s}^{-1}$. Both components are presumably associated with L1204, and have clear CO counterparts (Fig. 2 – Blair et al. 1978; Evans et al. 1987; Sugitani & Fukui 1987; Park & Minh 1995). There is also an isolated absorption feature towards the southeast, at $V_{LSR} \sim -2.5 \text{ km s}^{-1}$. Given its low LSR velocity, this feature is likely unrelated to L1204, and is probably a local cloud along the line of sight. Thus, while Sugitani & Fukui (1987) identified three molecular components associated with L1204 in their ^{13}CO observations, we only find two in our formaldehyde data. We do find evidence, however, for a systematic velocity gradient across the cloud. Park & Minh (1995) argued that this complex overall spatio-kinematical morphology was created when S140 and L1204 were swept up by an expanding shell associated with the Cepheus bubble. Our data do not illuminate this assertion any further, and a more thorough study is necessary to understand the detailed structure of this region.

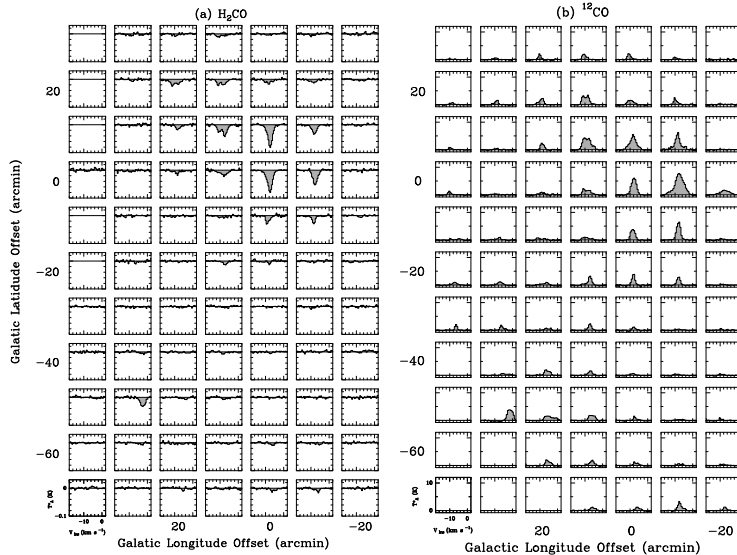


Fig. 2.— (a) Mosaic of H_2CO CMB absorption spectra observed in the L1204/S140 region. The (0,0) position corresponds to $l = 107^\circ.0$, $b = 5^\circ.3$, about $12'$ east of S140, and about $40'$ north-west of the nominal center of L1204 (Lynds 1962). (b) Corresponding $\text{CO}(1-0)$ observations smoothed to $10'$ (see text). Note that the CO emission is located a full $10'$ west of the maximum H_2CO absorption.

4. Comparison with other molecular tracers

The S140/L1204 region has been observed in many different molecular tracers (e.g. Tafalla et al. 1993, Zhou et al. 1993, Park & Minh 1995), but most of these observations have focused either on the S140 PDR or on the embedded infrared sources located just behind S140, while only a few observations covered the entire dust cloud. Indeed, the first CO observations of S140 (Blair et al. 1978) only covered a limited part of the region. To our knowledge, the only existing large-scale CO map of L1204 is that obtained in the 90s with the FCRAO telescope (see §2) and published by Heyer et al. (1996) and Helfer & Blitz (1997)¹. As mentioned earlier, we will use a smoothed version of that dataset here in order to compare with our formaldehyde observations.

In general, the CO emission and H_2CO absorption morphologies in this region are quite similar (Fig. 3). This was already noticed by Blair et al. (1978) in their $6'$ observations. It is also in good agreement with the results obtained towards the Galactic anticenter by

¹The region lies on the edge of, and is only partly covered by, the CfA Galactic plane survey of Dame et al. (2001).

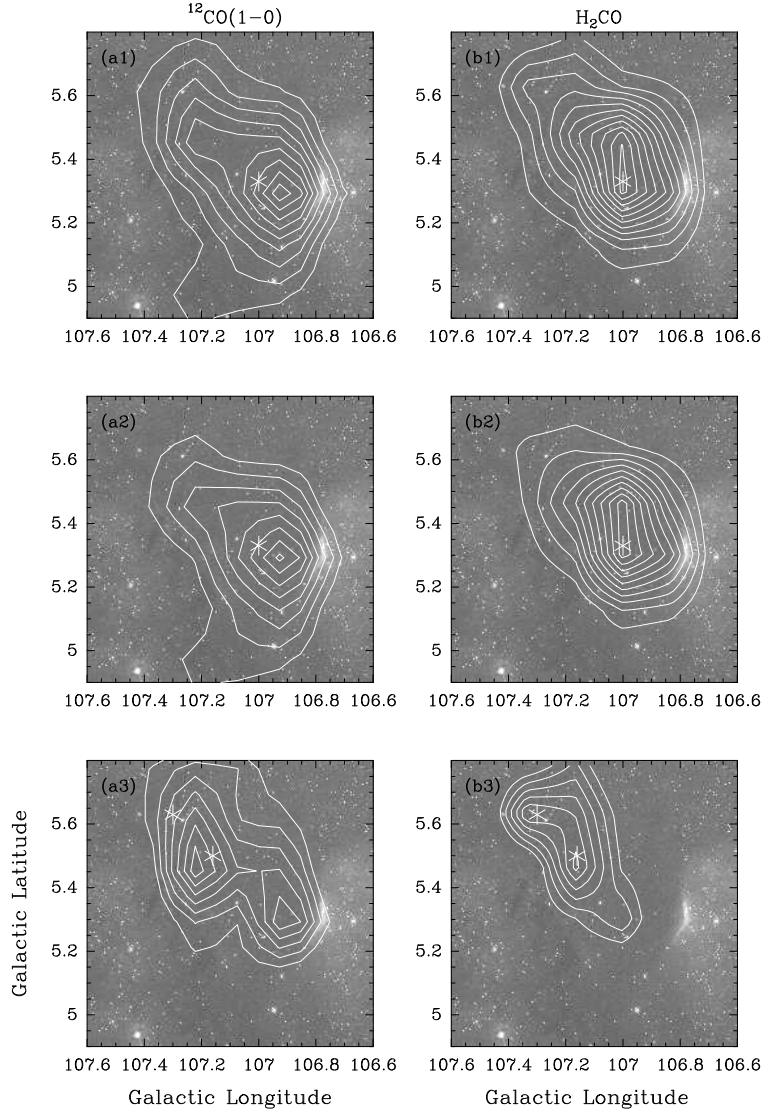


Fig. 3.— All panels show a grey-scale version of the DSS-red image of the region around $l = 107^\circ 0$, $b = 5^\circ 4$. The H_α arc of S140 is clearly visible on these (red) images near $l = 106^\circ 8$, $b = 5^\circ 3$. In the three left panels (a1–a3), CO contours taken from the smoothed CO data of Heyer et al. (1996) are overlaid on top of the DSS image, whereas in the three right panels (b1–b3), our H_2CO contours are overlaid. The contours in the top two panels (a1–b1) include the entire velocity range associated with L1204 (from -12 to -5 K km s^{-1}), whereas in the middle two (a2–b2) and bottom two (a3–b3) panels, the contours correspond only to the -11 K km s^{-1} and the -8 K km s^{-1} components, respectively. The asterisks correspond to the position of the peak H_2CO absorption for each component.

Rodríguez et al. (2006), and towards the Orion molecular complex by Cohen et al. (1983). There are, however, several noteworthy differences between the CO emission and H₂CO absorption in S140. The first difference is the fact that the CO peak and the H₂CO absorption maximum are not located at the same position. The CO integrated intensity map (Fig. 3, see also Fig. 2) shows that the maximum CO emission occurs just behind the S140 H α arc at the western edge of L1204, while only comparatively fainter emission extends to greater longitudes. The maximum H₂CO absorption, however, is located about 10' eastward of the CO peak. A second notable difference between the CO and H₂CO profile is the existence of a CO emission "tail" in the south/southeast part of the main cloud with little or no H₂CO counterpart (Figs. 2 and 3).

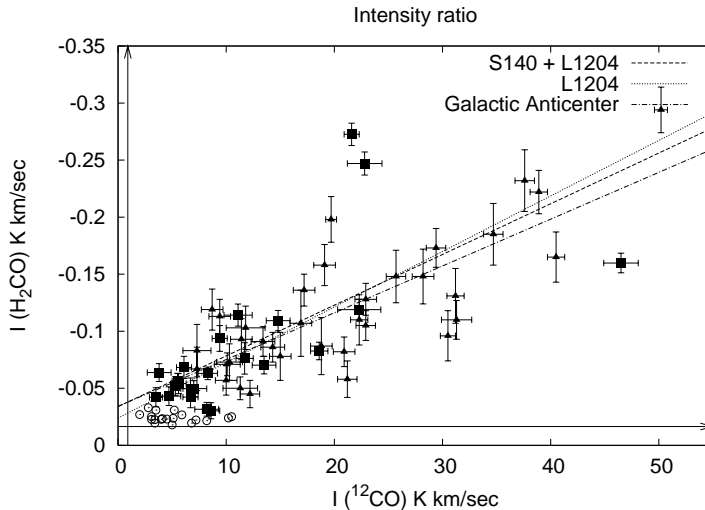


Fig. 4.— Correlation between the H₂CO absorption line intensity and the ¹²CO(1-0) emission line intensity at corresponding points in L1204. The squares correspond to data from Table 2, the open circles correspond to H₂CO upper limits and the triangles correspond to the Galactic anticenter data previously published in Rodríguez et al. (2006). The horizontal and vertical lines show the “best case” detection limit. The dashed line is the least-squares fit for the L1204/S140 region data, and the dash-dotted line is the least-squares fit for the Galactic anticenter data from Rodríguez et al. (2006). Note that the fits do not pass through the (0,0) point, suggesting that the relation is not linear at low intensity values.

In order to study the relation between H₂CO absorption and CO(1-0) emission in a more quantitative way, we have computed the moments of the profiles shown in Fig. 2. The results are listed in Table 2 (Appendix B). When two velocity components are visible at a given pointing, the moments for each were computed separately. Intensities above 3 σ are shown as squares in Fig. 4, and were used to make least-square fits (see below). The two

spatio-kinematical components that we identified in our formaldehyde dataset behave quite similarly with respect to the CO-H₂CO relation, and are plotted together in Fig. 4. The best least-squares fit to a straight line for the entire L1204 dataset yields:

$$I(H_2CO) = (4.4 \pm 1.1) \times 10^{-3} I(CO) + (34 \pm 16) \times 10^{-3} \text{ K km s}^{-1}. \quad (1)$$

We shall see momentarily that the CO emission near S140 may be particularly bright because of local heating. Ignoring the pointings very near S140, however, yields a fairly similar relation between CO and H₂CO:

$$I(H_2CO) = (3.8 \pm 0.9) \times 10^{-3} I(CO) + (31 \pm 9) \times 10^{-3} \text{ K km s}^{-1}. \quad (2)$$

The small difference between these relations presumably reflects the differing excitation requirements for the two lines. The relation between CO and H₂CO given by Eqs. 1 and 2 for the L1204 region is almost identical to that found towards the Galactic anticenter by Rodríguez et al. (2006):

$$I(H_2CO) = (4.1 \pm 0.5) \times 10^{-3} I(CO) + (34 \pm 13) \times 10^{-3} \text{ K km s}^{-1}. \quad (3)$$

It is important to note, however, that, in spite of the agreement between the fits to the Galactic anticenter and S140 data, there is very significant scatter in the CO-H₂CO relation, some points lying nearly 10σ away from the linear relation. This situation was already noticed by Rodríguez et al. (2006) in their study of the Galactic anticenter. This lack of a detailed correspondence between CO emission and H₂CO absorption presumably reflects differences in the excitation conditions of the two tracers, as we will now discuss in the next section.

5. Discussion

The comparison between H₂CO absorption and CO(1-0) emission profiles in the Galactic Anticenter and in the L1204/S140 region has led us to three important observational conclusions:

1. Qualitatively, the morphology of CO and H₂CO are quite similar, and quantitatively, the line integrated intensities correlate quite well with one another.

2. The scatter in the CO-H₂CO relation is, however, significantly larger than the observational errors.
3. In the specific case of S140, the CO emission peak is offset by about 3 pc from the locus of the deepest formaldehyde absorption, and there is a region south of the main cloud where significant CO emission is detected with little or no H₂CO counterpart.

From the general large-scale correspondance between the CO(1-0) and H₂CO 6 cm integrated maps (Fig. 3), and from the fair correlation between their line intensities (Fig. 4), we conclude that the physical conditions needed for the excitation of both lines are quite similar. The calculations presented in the Appendix A, indeed show that both lines preferentially trace warm gas at intermediate densities ($10^{3.6} < n < 10^5$ for H₂CO; $n > 10^{2.8}$ for CO). In this scheme, the offset between the CO(1-0) peak and the H₂CO maximum absorption may seem puzzling. Note that a similar trend is seen at higher resolution: while the CO peak in the full-resolution CO map published by Heyer et al. (1996) and Helfer & Blitz (1997) is at $l = 106^\circ.8$, $b = +5^\circ.3$, the H₂CO absorption feature seen in the high-resolution VLA images published by Evans et al. (1987) is centered around $l = 106^\circ.9$, $b = +5^\circ.3$, again a few arcminutes to the east.

We suggest that a combination of two effects may explain this puzzling result. First, it can be seen from the excitation analysis presented in Appendix A that the H₂CO absorption strength "saturates" for $T \gtrsim 30$ K, whereas the temperature of the CO emission continues to rise at higher kinetic temperature (Fig. 5). For example, while the H₂CO line strength increases by only about 30% when the kinetic temperature goes from 20 to 40 K, the CO(1-0) line intensity increases by more than a factor of two. According to Park & Minh (1995), the CO brightness temperature is about 40 K at the peak and 20 K for the rest of the cloud. Thus, the strong CO peak behind S140 may well be largely due to enhanced kinetic temperatures related to local heating (by the external star providing the ionization of S140, and/or by the infrared sources embedded in the cloud). As one progresses into the cloud, the local heating diminishes, and the CO line intensity fades. Also, it should be pointed out that the formaldehyde calculations presented in the Appendix show that the 6-cm line should be seen in emission rather than absorption when the density exceeds 10^5 cm^{-3} . The fact that this is not the case near the CO peak (neither in our low-resolution data, nor in the high-resolution VLA data presented by Evans 1978) suggests that the gas density there is lower than 10^5 cm^{-3} . Other effects that could explain the offset between the CO and the H₂CO peaks are the lower dissociation energy, and the lower abundance (and, therefore, lower self-shielding) of formaldehyde compared to CO (see Appendix A.3). In a photo-dissociated region, these effects should combine to create a stratified distribution where CO survives nearer the source of the UV photons than H₂CO. This stratification, combined with the heating of the CO,

would naturally lead to the offset between H₂CO and CO seen in the present data.

Finally, the origin of the other main difference between CO and H₂CO in S140, namely the existence of CO emission at the south of L1204 with no or little formaldehyde counterpart, is likely related to another aspect of the excitation differences between the 6 cm line of formaldehyde and the 1-0 transition of carbon monoxide. Fig. 6 of the Appendix A.2 shows that the density detection limit for H₂CO line is ~ 10 times larger than the density limit for the CO(1-0) line. We therefore suggest that the gas traced by the CO emission to the south of L1204 is of relatively very low density. It is interesting to note, indeed, that classical high-density molecular tracers (e.g. CS or NH₃) have only been detected around the CO peak behind S140, and not in the southern region of the cloud.

Thus, we conclude that the CO(1-0) and H₂CO 6 cm lines both tend to preferentially trace warm gas at intermediate densities. There are, however, significant differences related either to differing excitation requirements or to differing abundances. These differences can easily explain the large scatter in the CO–H₂CO relation.

6. Conclusions

The main conclusions of this work are the following:

1. We have mapped a large region ($70' \times 110'$) around L1204/S140 in the 6 cm line of formaldehyde, observing a total of 72 regularly-spaced positions every $10'$ on a regular grid. The center of our map was at $l = 107^\circ 0$, $b = +5^\circ 3$, and formaldehyde was detected against the cosmic microwave background in at least 16 of our 72 positions (Fig. 2).
2. The formaldehyde emission can be separated in three spatio-kinematical components (Fig. 3): two (at $V_{LSR} \sim -11$ km s⁻¹ in the northeast part of the cloud, and at $V_{LSR} \sim -8$ km s⁻¹ just behind S140) are clearly associated with L1204, whereas the other (an isolated component at $V_{LSR} \sim -2.5$ km s⁻¹ towards the southeast) is most likely a local foreground cloud unrelated to S140/L1204.
3. Both qualitatively and quantitatively, the CO(1-0) emission and the formaldehyde 6 cm absorption lines correlate fairly well. An excitation analysis shows that both preferentially trace warm gas at intermediate densities.
4. There are, however, notable differences between the CO and H₂CO lines, that can be traced to differing excitation requirements and abundances. Those differences are most likely the origin of the large scatter in the CO–H₂CO intensity correlation.

We thank Professor Roy Booth, director (retired) of the radio observatory at Onsala, for generous allocations of telescope time and for his warm hospitality during our several visits to the observatory. We are also grateful to the observatory technical and administrative staff for their capable assistance with our observing program. We thank Tamara Helfer for supplying us with the CO data cube of S140. We acknowledge the financial support of the *Dirección General de Asuntos del Personal Académico* (DGAPA), *Universidad Nacional Autónoma de México* (UNAM) and *Consejo Nacional de Ciencia y Tecnología* (CONACyT), in México, and the Director’s Discretionary Research Fund at the Space Telescope Science Institute. The Digitized Sky Surveys were produced at the Space Telescope Science Institute under U.S. Government grant NAG W-2166. The images of these surveys are based on photographic data obtained using the Oschin Schmidt Telescope on Palomar Mountain and the UK Schmidt Telescope. The plates were processed into the present compressed digital form with the permission of these institutions.

A. Model calculations

A.1. Collisional pumping

Observations of H_2CO in dark clouds show that the anomalous absorption of the 6 and 2 cm lines is due to collisions with H_2 that selectively overpopulate the lower levels of the lines (Evans et al. 1975). We calculated the non-LTE equilibrium populations of the first 40 levels of ortho- H_2CO assuming excitation by the 2.7 K background and collisions with H_2 . Green (1991) has calculated excitation rates of these levels for collisions with He taking advantage of the spherical symmetry of the He potential for kinetic temperatures $T = 10$ to 300 K. According to Green (1991), excitation rates by H_2 collisions could be 2.2 times higher than those by He because of the smaller reduced mass and differences in the interaction potentials. We will show the results of the calculations under the assumption that the H_2 - H_2CO collisional rates are the same as the He- H_2CO rates. Probabilities for the radiative transitions were taken from Jaruschewski et al. (1986).

The optical depths of the transitions involved in the pumping mechanism are generally larger than 1 at high densities and a radiative transfer calculation is required. Two limiting approximations in the radiation transport are often considered in molecular clouds: the large velocity gradient (LVG) model and the microturbulent model (Leung & Liszt 1976). The LVG model assumes that the line profile is dominated by systematic motion of the gas while the microturbulent model assumes that the turbulent velocity is much larger than any systematic motion. S 140 is likely to have several velocity components, but the existence of large systematic motions in molecular clouds and the validity of the LVG model has not

been well established in other molecular clouds (e.g. Evans et al. (1975), Zuckerman & Evans (1974), Zhou et al. (1990)). We therefore use the microturbulent model, and for simplicity we will use the escape probability formalism to account for photon trapping in a turbulent medium in plane-parallel slab of mean total optical depth τ_t that is perpendicular to the line of sight. In this case the A-value of a transition in the equations of statistical equilibrium is multiplied by a “loss probability” $P(\tau, \tau_t)$ that depends on the mean optical depth τ in the slab. There are many different ways to define $P(\tau, \tau_t)$, which can differ by several orders of magnitude for large optical depths. We will use the form suggested by Hummer & Storey (1992) for a uniform medium with no continuum absorption:

$$P(\tau, \tau_t) = \frac{1}{2}[K_2(\tau) + K_2(\tau_t - \tau)] , \quad (\text{A1})$$

where

$$K_2(\tau) = \int_{-\infty}^{\infty} dx \phi(x) E_2[\tau \phi(x)] , \quad (\text{A2})$$

and E_2 is the second exponential integral function. The function $K_2(\tau)$ can be calculated from fits by Hummer (1981) for a normalized Doppler profile, $\phi(x) = \exp(-x^2)/\sqrt{\pi}$.

Equation (A1) can be viewed as the single flight escape probability through either side of the slab averaged over the line profile. The probability that a photon of an isotropic background reaches optical depth τ in this slab is also given by equation (A1), and the blackbody continuum is thus attenuated by a factor $P(\tau, \tau_t)$. The mean optical thickness is given by

$$d\tau = \frac{\sigma_{lu}}{\Delta\nu_D} n_l \left(1 - \frac{n_u/g_u}{n_l/g_l} \right) dz , \quad (\text{A3})$$

where σ_{lu} is the absorption cross section of the transition and $\Delta\nu_D$ is the Doppler width. We assumed a Doppler width of 2 km s^{-1} (FWHM = $2\sqrt{\ln 2}\Delta\nu_D = 3.3 \text{ km s}^{-1}$). The level population and its statistical weight are given by n and g respectively with subindex u for the upper and l for the lower level.

The emergent line brightness temperature with subtracted background T_0 is found by direct integration of the source function throughout the slab as

$$\begin{aligned} \Delta T_b &= T_b - T_0 \\ &= T_0[\exp(-\mathcal{T}) - 1] \\ &+ \frac{h\nu}{k} \int_0^{\mathcal{T}} \exp(-\mathcal{T} + \tau) \left(\frac{n_l/g_l}{n_u/g_u} - 1 \right)^{-1} d\tau , \end{aligned} \quad (\text{A4})$$

where

$$\tau_t = \int_0^L \frac{\sigma_{lu}}{\Delta\nu_D} n_l \left(1 - \frac{n_u/g_u}{n_l/g_l} \right) dz, \quad (\text{A5})$$

is the total mean optical depth of a slab of thickness L and $\mathcal{T} = \tau_t \phi(0)$ is the line-center total optical depth.

Equation A4 gives the correct asymptotic limits: $T_b \rightarrow T_0$ when the density goes to 0 and $T_b \rightarrow T$ for high densities. The population densities and the optical depths as a function of position in the slab in equations (A1) and (A3) were calculated iteratively. A convergence of 10^{-3} K in T_b was achieved after a few iterations for $T \leq 40$ K and H_2 densities $n(\text{H}_2) < 10^6 \text{ cm}^{-3}$. For higher densities and temperatures the procedure becomes unstable. Fig. 5 shows the calculated ΔT_b for a 1 pc-thick slab as a function of the H_2 density and a constant H_2CO abundance of 2×10^{-9} with respect to H_2 (Hasegawa et al. (1992), Leung et al. (1984)). The assumed thickness of the slab has an important effect in the anomalous absorption as shown in Fig. 5. As the thickness of the slab decreases, the effectiveness of the pumping mechanism that cools the line decreases.

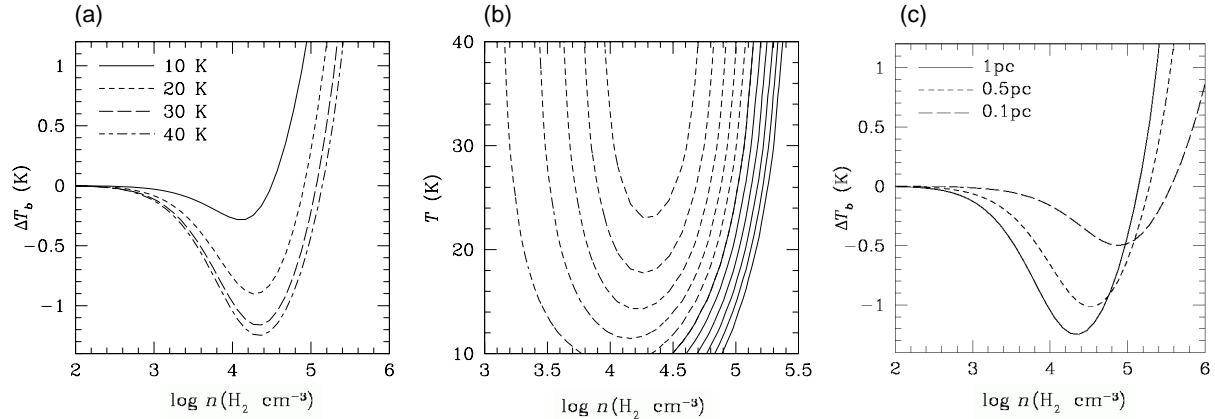


Fig. 5.— (a) Brightness temperature minus background continuum vs. density for different kinetic temperatures T of a 1-pc thick slab. (b) Contour intervals are 0.2 K from $\Delta T_b = -1$ to 1 K. (c) Brightness temperature minus background continuum vs. density for different slab thicknesses at $T = 40$ K.

Garrison et al. (1975) identified some transitions, like $1_{11} \rightarrow 3_{12}$, that produce selection effects in the excitation of some levels that cool the H_2CO doublets. We have tested our model for possible variations of the collision rates. An overall increase of collisional rates by a factor of 2.2 decreases ΔT_b in figure 5 by 0.3 to 0.5 K for $T \geq 20$ K and $n(\text{H}_2) > 1.6 \times 10^4 \text{ cm}^{-3}$. For lower T and $n(\text{H}_2)$ there is very little variation in the predicted T_b .

A.2. A PDR model for CO

The UV field has a higher influence on the CO brightness temperature than on the H₂CO brightness temperature. Both molecules are quickly photodissociated near the edge of clouds, but the larger abundance of the CO molecule makes its chemistry and interaction with radiation more complex. In order to take into account the variation of CO abundance along the line of sight, we used the Meudon PDR code to calculate the CO brightness temperature of a plane–parallel slab irradiated by a UV field (Le Bourlot et al. 1993). A detailed description of a revised version of the code is given by Le Petit et al. (2006).

The sharp separation between the molecular, atomic and ionized emissions suggests that the L1204/S140 interface is a PDR viewed nearly edge–on (Hayashi & Murata 1992) irradiated by HD 211880. The angle of incidence of the star’s radiation on the PDR boundary is an unknown parameter but appears to be more-or-less perpendicular. Furthermore, the infrared embedded sources are probably young stars that may also enhance the radiation field (Evans et al. 1989).

We ran the code with its parameters set to represent a plane–parallel slab irradiated from one side by a UV field with an enhancement factor $\chi = 200$ with respect to the Draine (1978) average interstellar radiation field. In a PDR, the gas is heated by the photoelectric emission from grains and PAH’s, H₂ formation in grains, UV pumping in the Lyman and Werner bands, gas–grain collisions, photoionization, and photodissociation. As the UV radiation is absorbed deeper into the cloud, other processes like cosmic rays and chemical reaction energies become important. Cooling is produced by fine–structure and molecular line emission. Shocks and turbulence can keep a PDR away from isobaric equilibrium. However in our model the temperature and density of the PDR were kept constant in order to compare the results with our H₂CO model in Fig. 6. We used the chemical network given for S140 by the Meudon group at its Internet site², which does not include H₂CO. Thus the CO and H₂CO calculations represent different models, and Fig. 6 is given only as indication of the local conditions that produce the emission and absorption for each molecule.

A.3. Photodissociation of H₂CO

The H₂CO molecule is quickly photodissociated into CO and H₂ or H in the average UV interstellar radiation field with a rate of $1.0 \times 10^{-9} \exp(-1.7A_V) \text{ s}^{-1}$ (van Dishoeck 1988). Keene et al. (1985) estimated that far–ultraviolet radiation (FUV) from the star HD211880

²<http://aristote.obspm.fr/MIS/pdr/exe.html>

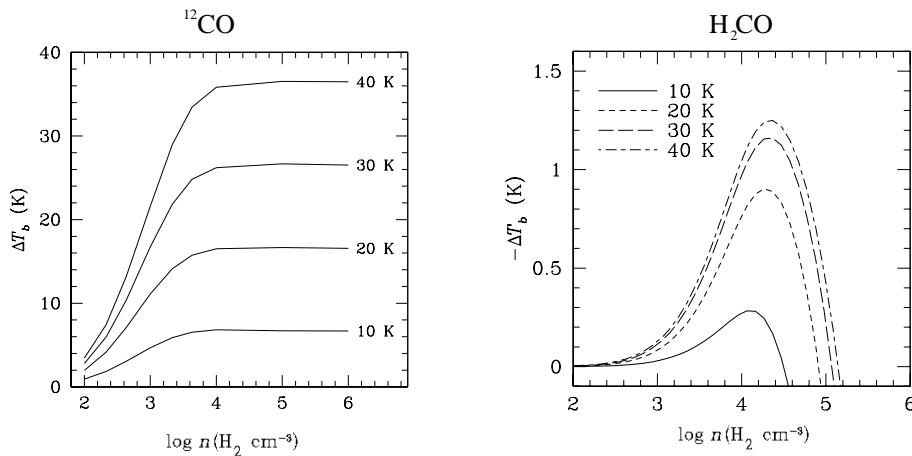


Fig. 6.— Brightness temperature minus background continuum vs. density for different kinetic temperatures T for both the $^{12}\text{CO}(1-0)$ and the 6 cm H_2CO line (Note that $\Delta T_b(k)$ is plotted "negative" compared to Figure 5).

will have an enhancement factor of $G_0 = 150$ with respect to the average interstellar field (Habing 1968) at the ionization front, although Spaans et al. (1997) found that a more intense radiation field may be needed to explain the H_2 rotational emission. H_2CO has a dissociation energy of $3.61 \pm 0.03 \text{ eV}$ (Suto Wang & Lee 1986), and a photodissociation rate of $1.0 \times 10^{-9} \text{ sec}^{-1}$ in the interstellar field (van Dishoeck 1988) while for CO the values are 11.2 eV and $2.0 \times 10^{-10} \text{ sec}^{-1}$ respectively. Thus it is possible that the H_2CO will be selectively photodissociated near the S140 ionization front and the bright PDR region, where the CO emission peaks. Detailed PDR model calculations by Li et al. (2002) show that at $20'$ from the ionization front, where we observe the H_2CO maximum, $G_0 \leq 20$ and $A_V \sim 15$.

We added 62 reactions involving H_2CO and H_2CO^+ taken from the UMIST data base (Woodall et al., 2007)³ to the chemical network of the Meudon group mentioned above and ran a PDR model with $G_0 = 200$, $T = 40\text{K}$ and constant density of 10^3 cm^{-3} . We found that H_2CO has significant abundance only at depths of $A_v > 7$ while CO becomes important at $A_v > 4$, which shows that photodestruction could explain the offset between the CO and the H_2CO peaks.

³<http://www.udfa.net/>

B. Profile moments in detail

Table 2. Profile moments for each position of Fig. 2. The upper limits correspond to 3σ . The symbol “...” indicates no data were available, while “nf” indicates that data were available but no reliable fit could be made. Values marked with “yes” in column 6 are plotted as squares in Fig. 4, and were used for the least square fits.

Offset (l, b) arcmin	$1000 \times I(\text{H}_2\text{CO})$ K km s $^{-1}$	$\langle V \rangle$ km s $^{-1}$	$I(\text{CO})$ K km s $^{-1}$	$\langle V \rangle$ km s $^{-1}$	Included in fits
40, -70	< -24.3	nf	
30, -70	< -18.9	nf	
20, -70	< -25.8	nf	
10, -70	< -23.4	nf	4.1 ± 0.7	-7.6 ± 1.3	
0, -70	-42.1 ± 8.4	-7.5 ± 1.5	3.5 ± 0.6	-8.7 ± 1.5	yes
-10, -70	-30.3 ± 7.1	-6.2 ± 1.5	8.6 ± 0.8	-8.3 ± 0.8	yes
-20, -70	< -21.6	nf	< 2.1	nf	
40, -60	< -22.5	nf	
30, -60	< -24.0	nf	
20, -60	< -26.7	nf	5.9 ± 0.8	-7.0 ± 1.1	
10, -60	< -23.7	nf	5.1 ± 0.6	-8.3 ± 1.0	
0, -60	< -19.2	nf	< 1.8	nf	
-10, -60	-27.9 ± 7.1	-6.7 ± 0.5	< 2.1	nf	
-20, -60	< -28.8	nf	< 1.5	nf	
40, -50	< -25.5	nf	
30, -50	-109.3 ± 8.9	-2.6 ± 0.2	14.8 ± 1.1	-1.8 ± 0.2	yes
20, -50	< -25.2	nf	10.5 ± 0.8	-5.0 ± 0.4	
10, -50	< -21.6	nf	8.2 ± 0.6	-7.0 ± 0.5	
0, -50	< -18.9	nf	< 2.4	nf	
-10, -50	< -16.5	nf	< 2.4	nf	
-20, -50	< -24.6	nf	< 4.8	nf	
40, -40	< -23.1	nf	
30, -40	< -22.8	nf	3.1 ± 0.6	-6.2 ± 1.2	
20, -40	< -22.2	nf	7.2 ± 0.8	-7.2 ± 0.9	
10, -40	< -23.1	nf	4.5 ± 0.5	-8.8 ± 1.1	
0, -40	< -22.5	nf	< 2.7	nf	
-10, -40	< -26.1	nf	< 2.7	nf	
-20, -40	< -18.6	nf	< 3.0	nf	
40, -30	< -22.5	nf	3.4 ± 0.5	-9.0 ± 1.5	
30, -30	< -22.8	nf	4.0 ± 0.7	-8.9 ± 1.5	

Table 2—Continued

Offset (l, b) arcmin	$1000 \times I(\text{H}_2\text{CO})$ K km s ⁻¹	$\langle V \rangle$ km s ⁻¹	$I(\text{CO})$ K km s ⁻¹	$\langle V \rangle$ km s ⁻¹	Included in fits
20, -30	< -25.5	nf	< 1.8	nf	
10, -30	< -30.9	nf	5.2 ± 0.6	-8.6 ± 1.0	
0, -30	< -20.1	nf	< 4.2	nf	
-10, -30	< -26.7	nf	< 1.8	nf	
-20, -30	< -22.2	nf	< 2.1	nf	
40, -20	< 2.7	nf	
30, -20	< -30.9	nf	3.5 ± 0.7	-9.4 ± 1.9	
20, -20	< -24.0	nf	< 2.7	nf	
10, -20	-31.6 ± 6.0	-8.2 ± 1.6	8.2 ± 1.1	-8.9 ± 1.2	yes
0, -20	< -29.1	nf	8.5 ± 1.4	-9.5 ± 1.7	
-10, -20	< -19.5	nf	6.8 ± 0.3	-8.7 ± 0.9	
-20, -20	< -22.2	nf	< 1.5	nf	
40, -10	< 1.8	nf	
30, -10	< -35.7	nf	< 2.4	nf	
20, -10	< -16.8	nf	< 3.0	nf	
10, -10	-43.1 ± 8.2	-8.1 ± 1.6	4.7 ± 1.1	-10.3 ± 2.8	yes
0, -10	-76.2 ± 13.8	-9.5 ± 1.8	11.7 ± 0.8	-9.0 ± 0.6	yes
-10, -10	-82.7 ± 7.7	-8.1 ± 0.8	18.6 ± 0.6	-8.2 ± 0.3	yes
-20, -10	< -24.3	nf	< 2.7	nf	
40, 0	< -33.0	nf	2.8 ± 0.5	-11.6 ± 2.3	
30, 0	< -28.8	nf	< 3.3	nf	
20, 0	-63.8 ± 7.8	-7.8 ± 0.9	3.8 ± 1.1	-8.9 ± 3.0	yes
10, 0	-93.7 ± 11.3	-8.7 ± 1.1	9.4 ± 0.7	-9.9 ± 0.8	yes
0, 0	-272.6 ± 9.8	-7.8 ± 0.3	21.6 ± 0.7	-8.0 ± 0.3	yes
-10, 0	-159.8 ± 8.6	-8.0 ± 0.4	46.5 ± 1.6	-7.8 ± 0.3	yes
-20, 0	< -24.0	nf	10.2 ± 0.7	-7.7 ± 0.6	
40, +10	< 1.7	nf	
30, +10	< -28.8	nf	< 0.9	nf	
20, +10	-52.0 ± 8.2	-8.7 ± 1.4	5.3 ± 0.4	-9.1 ± 0.7	yes
10, +10	-114.1 ± 9.7	-6.2 ± 0.6	11.1 ± 1.3	-7.1 ± 0.9	yes

Table 2—Continued

Offset (l, b) arcmin	$1000 \times I(\text{H}_2\text{CO})$ K km s ⁻¹	$\langle V \rangle$ km s ⁻¹	$I(\text{CO})$ K km s ⁻¹	$\langle V \rangle$ km s ⁻¹	Included in fits
	-70.3 ± 7.7	-10.3 ± 1.2	13.5 ± 1.1	-10.6 ± 1.0	yes
0, +10	-247.0 ± 10.1	-7.6 ± 0.3	22.8 ± 1.6	-8.5 ± 0.6	yes
-10, +10	-118.9 ± 9.2	-8.1 ± 0.6	22.3 ± 2.0	-8.6 ± 0.8	yes
-20, +10	< -19.2	nf	< 0.9	nf	
40, +20	< 1.2	nf	
30, +20	< -25.2	nf	3.1 ± 0.4	-8.3 ± 1.7	
20, +20	-42.3 ± 9.3	-7.1 ± 1.6	6.7 ± 0.7	-9.9 ± 1.0	yes
	-82.0 ± 7.4	-11.3 ± 1.1	nf	nf	
10, +20	-49.8 ± 6.9	-6.9 ± 1.0	7.0 ± 1.2	-8.0 ± 1.4	yes
	-63.1 ± 5.5	-10.8 ± 1.0	8.3 ± 0.9	-11.0 ± 1.4	yes
0, +20	-68.3 ± 9.7	-8.9 ± 1.3	6.1 ± 0.7	-10.8 ± 1.3	yes
-10, +20	-56.4 ± 6.8	-8.6 ± 1.1	5.5 ± 0.5	-10.8 ± 1.1	yes
-20, +20	< -29.7	nf	< 2.7	nf	
40, +30	< 1.6	nf	
30, +30	< -27.9	nf	< 1.6	nf	
20, +30	< -19.5	nf	3.4 ± 0.8	-11.4 ± 2.7	
10, +30	-54.1 ± 8.8	-9.3 ± 1.6	5.6 ± 0.7	-10.3 ± 1.2	yes
0, +30	< -18.0	nf	5.0 ± 0.6	-11.1 ± 1.3	
-10, +30	< -27.0	nf	2.0 ± 0.4	-10.2 ± 2.2	
-20, +30	< -23.4	nf	< 3.0	nf	

REFERENCES

- Bally, J., Reipurth, B., Walawender, J., & Armond, T., 2002, *AJ*, 124, 2152
- Blair, G. N., Evans, N. J., Vanden Bout, P. A., & Peters W. L., 1978, *ApJ*, 219, 893-913
- Crampton, D., & Fisher, W. A., 1974, *Pub. Dom. Astrophys. Obs.*, 14, 283
- Cohen, R. J., Matthews, N., Few, R. W., & Booth, R. S., 1983, *MNRAS*, 203, 1123
- Dame, T. M., Hartmann, D., & Thaddeus, P., 2001, *ApJ*, 547, 792
- Draine, B. T., 1978, *ApJS*, 36, 595.
- Evans, N. J., II, Zuckerman, B., Sato, T., & Morris, G. 1975, *ApJ*, 199, 383.
- Evans, N. J., II, Rubin, R. H., & Zuckerman, B. 1980, *ApJ*239, 839
- Evans, N. J., II, Kutner, M. L., & Mundy, L. G., 1987, *ApJ*, 323, 145
- Evans, N. J., II, Mundy, L. G., Kutner, M. L.; Depoy, D. L., 1989, *ApJ*, 346, 212.
- Garrison, B. J., Lester, W. A., Jr., Miller, W. H., & Green, S., 1975, *ApJ*, 200, L175.
- Green, S. 1991, *ApJS*, 76, 979.
- Guilloteau S., & Forveille T. 1989, *Grenoble Image and Line Data Analysis System (GILDAS)*, IRAM, <http://www.iram.fr/IRAMFR/GILDAS>
- Habing, H. J., 1968, *Bull. Astron. Inst. Netherlands*, 19, 421.
- Hasegawa, T. I., Herbst, E., & Leung, C. M., 1992, *ApJS*, 82, 167.
- Hayashi M., & Murata Y., 1992, *PASJ*, 44, 391
- Hayashi, M. & Murata, Y., 1992, *PASJ*, 44, 391.
- Helfer, T. T., & Blitz, L., 1997, *ApJ*, 478, 233
- Heyer, M. H., Carpenter, J. M., & Ladd, E. F., 1996, *ApJ*, 463, 630
- Hummer, D. G., 1981, *J. Quant. Spec. Radiat. Transf.*, 26, 187.
- Hummer, D. G., & Storey, P. J., 1992, *MNRAS*, 254, 277.

- Jaruschewski, S., Chandra, S., Varshalovich, D. A., & Kegel, W. H. 1986, *A&AS*, 63, 307.
- Keene, J., Blake, G. A., Phillips, T. G., Huggins, P. J., & Beichman, C. A., 1985, *ApJ*, 299, 967.
- Le Bourlot, J., Pineau Des Forets, G., Roueff, E. & Flower, D. R., 1993, *å*, 267, 233.
- Le Petit, F., Nehmé, C., Le Bourlot, J. & Roueff, E., 2006, *ApJS*, 164, 506.
- Le Teuff Y. H., Millar T. J., & Markwick A. J., 2000, *A&AS*, 146, 157.
- Leung, C. M., & Liszt, H. S., 1976, *ApJ*, 208, 732.
- Leung, C. M., Herbst, E., & Huebner, W. F., 1984, *ApJS*, 56, 231.
- Li, W., Evans, N. J., II, Jaffe, D. T., van Dishoeck, E. F., & Thi, W. F., 2002, *ApJ*, 568, 242.
- Lynds, B. T., 1962, *ApJS*, 7, 1
- Park, Y., & Minh Y., 1995, *JKAS*, 28, 255
- Preibisch, T., Balega, Y. Y., Schertl, D., Smith, M. D., & Weigelt, G., 2001, *A&A*, 378, 539
- Preibisch, T., & Smith, M. D, 2002, *A&A*, 383, 540
- Rodríguez, M. I., Allen, R., Loinard, L., & Wiklind, T., 2006, *ApJ*, 652, 1230
- Sharpless, S., 1959 , *ApJS*, 4, 257
- Snyder, L. E., Buhl, D., Zuckerman, B., Palmer, P., 1969, *PhRvL*, 22, 679
- Spaans, M & van Dishoeck, E. F., 1997, *å*, 323, 953
- Sugitani, K., & Fukui, Y., 1987, *IAUS*, 115, 75
- Suto, M., Wang, X., & Lee, L.C., 1986, *JChPh*, 85, 4228
- Thaddeus, P., 1972, *ApJ*, 173, 317
- Tafalla, M., Bachiller, R., & Martin-Pintado, J., 1993, *ApJ*, 403, 175
- Timmermann, R., Bertoldi, F., Wright, C. M., Drapatz, S., Draine, B. T., Haser, L., & Sternberg, A., 1996, *A&A*, 315L, 281
- Townes, C. H., & Cheung, A. C., 1969, *ApJ*, 157L, 103

Ungerechts, H., Winnewisser, G., Walmsley, C. M., 1986, *A&A*, 157, 207

van Dishoeck, E. F. 1988, *Rate Coefficients in Astrochemistry*, Millar, T. J. & Williams, D. A. (ed.), Dordrecht: Kluwer, 1988, p. 49.

Vanden Bout, P. A., Snell, R. L., & Wilson, T. L., 1983, *A&A*, 118, 337

Zhou, S., Evans, N. J. II, Butner, H. M., Kutner, M. L., Leung, C. M., & Mundy, L. G., 1990, *ApJ*, 363, 168.

Zuckerman, B., Evans, N. J., II 1974, *ApJ*, 192, L149.